



Tailoring the mechanical and tribological properties of sputtered boron carbide films via the $B_1 - xC_x$ composition

J.C. Qian^{a,b}, Z.F. Zhou^c, C. Yan^a, D.J. Li^b, K.Y. Li^c, S. Descartes^{d,e}, R. Chromik^e, W.J. Zhang^a, I. Bello^f, L. Martinu^b, J.E. Klemberg-Sapieha^{b,*}

^a Department of Physics and Materials Science and Center of Super-Diamond and Advanced Films, City University of Hong Kong, Hong Kong Special Administrative Region

^b Department of Engineering Physics, École Polytechnique de Montréal, Montréal, Québec, Canada, H3C 3A7

^c Advanced Coatings Applied Research Laboratory (ACARL), Department of Mechanical and Biomedical Engineering, City University of Hong Kong, Hong Kong Special Administrative Region

^d Université de Lyon, CNRS, INSA-Lyon, LaMCoS, UMR 5259, F-69621, Villeurbanne, France

^e Department of Mining and Materials Engineering, McGill University, Montreal, Québec, Canada, H3A 0C5

^f Vacuum Electronics Ltd., London, Ontario, Canada

ARTICLE INFO

Available online 30 October 2014

Keywords:

Boron carbide films
Magnetron sputtering
Tribo-mechanical properties
Corrosion resistance

ABSTRACT

Boron carbide films are very attractive due to their high hardness and interesting tribological properties. In the present work, the compositional effect of boron carbide $B_1 - xC_x$ ($0 < x < 1$) films is systematically studied to tailor mechanical, tribological and corrosion properties of the films. The $B_1 - xC_x$ layers were deposited on Si (100) and M2 high speed steel substrates using a pilot-scale closed-field unbalanced magnetron sputtering system equipped with one graphite and two boron targets. Different compositions were obtained by tuning the electrical power applied to the graphite target. The hardness of the $B_1 - xC_x$ films decreases from 28 to 20 GPa as the carbon content [C] rises from 19 to 56 at.%, but thereafter it increases again up to ~25 GPa when [C] reaches 76 at.%. The hardness variation is explained by changes in the film microstructure, namely formation of either a nanocrystalline boron carbide in the case of boron-rich films, or boron carbide nanocrystals dispersed in an amorphous boron carbide/a-C matrix in the case of carbon-rich films as deduced from the combined XPS, micro-Raman and XRD measurements. The friction coefficient of the $B_1 - xC_x$ films reduces from 0.66 to 0.13, and the wear rate against alumina ball drops from $6.4 \times 10^{-5} \text{ mm}^3/\text{Nm}$ to $1.3 \times 10^{-7} \text{ mm}^3/\text{Nm}$ with increasing the [C]. Raman analyses indicate that improvement of the tribological properties of the $B_1 - xC_x$ films is primarily caused by the presence of the amorphous carbon phase that leads to the formation of a graphitic tribolayer acting as a solid lubricant during the wear process. Deposition of the $B_{0.81}C_{0.19}$ film with high hardness (28 GPa) improves the corrosion resistance of the M2 steel substrate by four orders of magnitude, documented by the decrease of the corrosion current from $3 \times 10^{-6} \text{ A/cm}^2$ to $8 \times 10^{-10} \text{ A/cm}^2$. We demonstrate that adjustment of the x-portion in the $B_1 - xC_x$ system allows one to tailor the tribo-mechanical properties over a large range from high hardness/high friction to high hardness/low friction structures.

© 2014 Elsevier B.V. All rights reserved.

1. Introduction

Boron carbide is well known for its excellent mechanical properties. With its hardness of ~40 GPa, it is the third hardest traditional bulk material at room temperature after diamond and cubic boron nitride, and it is a good candidate for mechanical applications at high temperature due to its high thermal stability [1]. The physical properties such as low mass density of 2.52 g/cm^3 (light weight material), low thermal expansion coefficient of $4.3 \times 10^{-6} \text{ K}^{-1}$, high thermal and chemical stability and good wear resistance, make boron carbide suitable for many industrial applications including hard disks, cutting tools, aerospace components, military armor products and others [2–4].

The detailed atomic structure of boron carbide is still ambiguous [5] since ^{11}B and ^{12}C cannot be well distinguished by X-ray and neutron diffraction due to their similarity in electron density and nuclear cross-section [5–9]. Its lattice structure is usually idealized as a rhombohedral unit cell, where one $B_{11}C$ icosahedra is located at each node of the lattice, and one linear C–B–C chain connects the nodes along the (111) axis [5,6]. However, the investigation of Raman spectra of boron carbide with the increasing carbon content showed that boron atoms in the icosahedra and in the chain could be substituted by carbon atoms. Even in monocrystalline boron carbide, small amount of carbon could be observed [10,11]. As a consequence, the electrical and mechanical properties are affected by the change in carbon concentration and chemical states [12].

Inspired by the attractive properties of the bulk boron carbide material, numerous studies focused on boron carbide films prepared by a

* Corresponding author. Tel.: +1 514 340 5747; fax: +1 514 340 3218.
E-mail address: jolanta-ewa.sapieha@polymtl.ca (J.E. Klemberg-Sapieha).

variety of deposition techniques such as chemical vapor deposition (CVD) [13–15], magnetron sputtering [16–18], ion beam assisted deposition [19] and pulsed laser deposition [3,20,21]. CVD deposited films were studied for their photoelectrical properties [22], while their hardness was found to vary considerably (typically from 22 GPa to 33 GPa [23]) depending on the composition and the deposition parameters; the high hardness is usually reached when the temperature is very high ($>1000\text{ }^{\circ}\text{C}$) [24]. In previous studies, boron carbide films with modulated carbon contents were deposited by reactive magnetron sputtering accompanied by continuously tuning the hydrocarbon gas to adjust the film structure and the mechanical properties [25,26]. However, addition of the hydrocarbon led to a decrease of hardness due to the trapped hydrogen.

The main aim of the present work is to fabricate $B_1 - xC_x$ films with x varied over a large range in order to tailor their tribo-mechanical properties. For versatility the films were sputtered from single element targets, boron and graphite. We demonstrate a possibility to tune their hardness, friction, wear and corrosion resistance by controlling the film composition and microstructure.

2. Experimental

2.1. Deposition of the $B_1 - xC_x$ films

$B_1 - xC_x$ films were deposited on Si (100) and high speed steel M2 substrates using a closed-field unbalanced magnetron sputtering system (UPD 450, Teer Coatings Ltd.) comprising four rectangular planar (with a size of $330\text{ mm} \times 133\text{ mm}$) unbalanced magnetrons in a $4 \times 90^{\circ}$ configuration. The $B_1 - xC_x$ films were obtained from one graphite target and two boron targets operated simultaneously, respectively powered by a DC power supply and two pulsed DC power supplies (350 kHz, 1 μs). A 200 nm TiB_2 interlayer was deposited on the M2 steel substrate prior to the $B_1 - xC_x$ films using a TiB_2 target powered by a DC power supply. The distance between the targets and the substrate was 70 mm. A cylindrical substrate holder rack rotating at 10 rpm was used to avoid a layered structure and provide a homogeneous compound. The total film thickness was 500 nm and 1 μm when deposited on Si and M2 steel substrates, respectively.

Prior to deposition, all the substrates were ultrasonically cleaned in baths of a detergent (Decon 90), ethanol and deionized water. After introduction to the deposition chamber, the substrate surface was sputter-cleaned for 30 minutes with Ar plasma at 250 kHz using a bias of -450 V . The system was pumped down to a background pressure $<1.0 \times 10^{-4}\text{ Pa}$ before the deposition. Sputtering was carried out in Ar plasma at a pressure of $1.86 \times 10^{-1}\text{ Pa}$ with an Ar flow rate of 15 sccm, ($2.72 \times 10^{-2}\text{ Pa}\cdot\text{m}^3/\text{s}$ at $20\text{ }^{\circ}\text{C}$). The boron target was sputtered at a constant power density of $2\text{ W}/\text{cm}^2$, while the graphite target power density was varied from $0.5\text{ W}/\text{cm}^2$ to $4\text{ W}/\text{cm}^2$. The substrate was biased at -60 V during the deposition, and the substrate temperature was maintained at $\sim 200\text{ }^{\circ}\text{C}$.

2.2. Structural and compositional characterization

The $B_1 - xC_x$ films were analyzed by several complementary techniques; this included: a) surface sensitive (10 nm) X-ray photoelectron spectroscopy (XPS) using a VG ESCALAB 220i-XL instrument equipped with a monochromatic Al $K\alpha$ (1486.6 eV) X-ray source; Ar ion beam sputtering with 3 keV Ar ions at an angle of 30° was used for 5 minutes to remove adventitious hydrocarbons and other carbon- and oxygen based contaminants adsorbed on the film surface. b) In depth sensitive (about $0.5\text{--}1.0\text{ }\mu\text{m}$) Rutherford backscattering spectrometry (RBS); c) Raman scattering spectra were measured by a Renishaw inVia Raman spectrometer with an excitation wavelength of 633 nm. The scattered light was collected in the backscattering geometry using a high sensitivity ultra-low noise CCD detector. d) The XRD patterns of the $B_1 - xC_x$ films were collected by a Philips X'Pert X-ray diffractometer

with Cu $K\alpha$ X-rays at a grazing angle of 2° in a Bragg–Brentano configuration.

2.3. Mechanical and tribological tests

The hardness (H) and reduced Young's modulus (E_r) of the $B_1 - xC_x$ films were determined by depth-sensing indentation using Triboindenter (Hysitron) system equipped with a Berkovich pyramidal tip. The measurements were performed on films prepared on Si substrates while applying a maximum load of 5 mN. All the data were analyzed using the Oliver and Pharr method [27], and the hardness was determined at an indentation depth less than 10% of the film thickness to reduce the error caused by substrate.

The friction coefficient, μ , of the $B_1 - xC_x$ films on the M2 steel substrates was measured by two types of pin-on-disk tribometers, using both linear reciprocating and rotating motion modes. A normal force of 2 N was applied to an alumina ball 6.35 mm in diameter being used as a counterpart friction material. In the reciprocating test, the wear track length, the linear speed and the sliding distance were 7 mm, 2.8 mm/s and 7 m, respectively. In the rotating test, the diameter of the wear track ring was 7 mm, the linear speed was 30 mm/s, and the sliding distance was 50 m. For each sample the friction was expressed by the mean friction coefficient, $\bar{\mu}$, during the 50 m sliding, and the error of μ was estimated by the standard deviation of all the experimental data. The wear rate K was calculated from the latter measurements as $K = V/(F \times s)$, where V is the worn volume measured by a profilometer, F is the normal load, and s is the sliding distance. Four measurements of V were performed on each wear track in order to reduce the random error.

2.4. Corrosion measurements

The corrosion properties were measured in an electrolyte (NaCl 1 wt.% solution) at room temperature using the Autolab PGSTAT302 potentiostat with a three-electrode cell type described elsewhere [28]. $B_1 - xC_x$ films on the M2 steel substrates were exposed to the electrolyte with a circular area of 10 mm in diameter (0.79 cm^2), while the substrate served as a working electrode. A standard calomel electrode and a graphite rod were used as reference and counter electrodes, respectively. The electrodes were first stabilized in the electrolyte for 1 hour to reach a stable open circuit potential (OCP) to reduce measurement error. Then the potentiodynamic polarization test was performed with a scan rate of 0.001 V/s, while the applied voltage varied from -0.2 V below the OCP to a potential when a current density of $1\text{ mA}/\text{cm}^2$ was reached.

3. Results

3.1. Chemical composition

In the first part of this work, we evaluate the effect of deposition conditions on the film composition, specifically to control the $[C]$ value. Fig. 1 shows $[C]$ in the $B_1 - xC_x$ films as a function of power density applied to the graphite target characterized by both XPS and RBS analyses. Comparing the results collected from these two techniques, it is found that the overall trend of the variation is very comparable for both approaches, but the carbon content measured by XPS is slightly higher than that detected by RBS. Indeed, RBS data are less affected by possible surface contamination by carbon, and they better represent the films' bulk composition. Therefore, the carbon content $[C]$ referred to below is that obtained by RBS. By tuning the graphite target power density from 0.5 to $4\text{ W}/\text{cm}^2$, the $B_1 - xC_x$ films exhibit $[C]$ change from 19 to 76 at.%. The concentration of oxygen in the $B_1 - xC_x$ films measured by RBS is around 2 at.%.

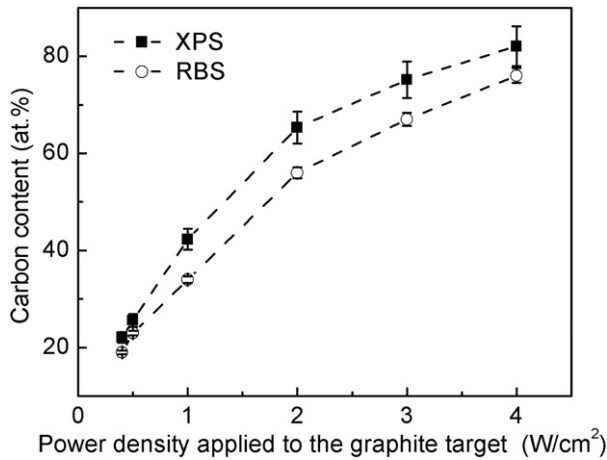


Fig. 1. Carbon content in the $B_1 - xC_x$ films as a function of the power density applied to the graphite target as evaluated by the XPS and RBS analytical techniques.

3.2. Mechanical properties

The mechanical properties of the $B_1 - xC_x$ films are presented in Fig. 2. Fig. 2(A) illustrates typical load–displacement curves for $B_{0.81}C_{0.19}$, $B_{0.44}C_{0.56}$ and $B_{0.24}C_{0.76}$ films, while the inset schematically describes the load–displacement curve and the methodology for the

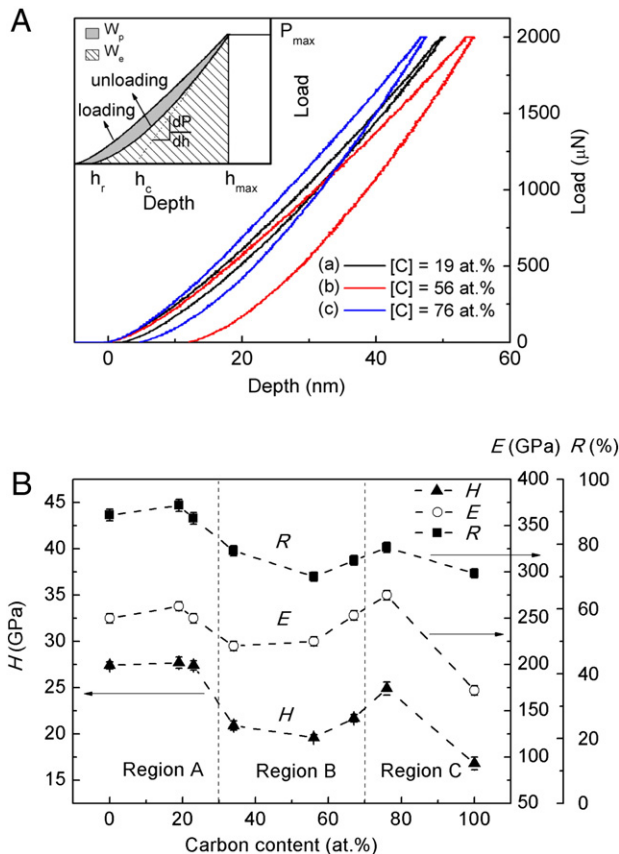


Fig. 2. (A) Load–displacement curves for the $B_1 - xC_x$ films with the $[C]$ contents of 19, 56, and 76 at.%; the inset presents a schematic representation of the load–displacement curve, where h_r is the depth of the residual impression, h_c is the contact depth, h_{max} is the maximal penetration depth, P_{max} is the maximum load, W_p is the plastic energy, and W_e is the elastic energy. (B) Hardness, Young's modulus, and elastic recovery of the $B_1 - xC_x$ films as a function of the carbon content.

determination of the hardness, Young's modulus, and elastic recovery, R . The hardness is defined as the indentation load divided by the projected contact area, $H = P_{max}/A_c$, where P_{max} is the maximum load, and A_c is the projected contact area equal to $24.5h_c^2$ for Berkovich indenter. The reduced Young's modulus can be calculated as $E_r = \frac{1}{2} \frac{\sqrt{\pi}}{\sqrt{A_c}} \frac{dP}{dh}$ while the

Young's modulus of the coatings can be extracted from the equation $\frac{1}{E_r} = \frac{(1-\nu^2)}{E} + \frac{(1-\nu_i^2)}{E_i}$, where E and E_i are elastic moduli of the sample and of the indenter, and ν and ν_i are the Poisson's ratios of the sample and the indenter [27].

The energy dissipated in the material due to plastic deformation, W_p , is represented by the area between the loading and unloading curves; in contrast, the energy due to elastic deformation, W_e , corresponds to the area under the unloading curve [29]. The elastic recovery is then calculated as $R = W_e/(W_p + W_e)$.

The $B_{0.81}C_{0.19}$ film exhibits the highest H value of 28 GPa and a high R of 92%. On the contrary, the $B_{0.24}C_{0.76}$ film with H of 25 GPa shows the smallest penetration depth at the maximum load, indicating high resistance to both plastic and elastic deformation. However, due to a lower R of 79%, the hardness, that is determined as the resistance to plastic deformation, is lower than that for the $B_{0.81}C_{0.19}$ film. The $B_{0.44}C_{0.56}$ film provides the lowest mechanical performance regarding to the combination of hardness, elastic recovery and the penetration depth.

The hardness and the Young's modulus of the $B_1 - xC_x$ films are plotted in Fig. 2(B) as a function of $[C]$. The H and E values of pure boron and carbon films, deposited from elemental boron and graphite targets, are also shown for reference. According to the variation trend of H and E , the mechanical behavior can be divided in three regions with respect to $[C]$: (i) region A where $[C] < 30$ at.%; (ii) region B where $30 \text{ at.}\% < [C] < 70$ at.%; and (iii) region C where $[C] > 70$ at.%. In the boron-rich region A the maximum H of 28 GPa occurs for $[C]$ around 20 at.%. In region B the overall hardness is lower, and it exhibits a minimum of 20 GPa for the $B_{0.44}C_{0.56}$ film. As the carbon content further increases (region C), the hardness reaches 25 GPa ($B_{0.24}C_{0.76}$ film). The overall variation trend of the Young's modulus and the elastic recovery as a function of $[C]$ exhibits a trend similar to that of the hardness. The mechanical behavior is interpreted in terms of the film microstructure in Section 3.4.

3.3. Tribological and electrochemical characteristics

In the following we evaluate the tribological properties of the $B_1 - xC_x$ films in order to assess their performance in the context of protective coating applications. As an example, Fig. 3(A) shows the evolution of the friction coefficient as a function of sliding distance for the $B_{0.81}C_{0.19}$, $B_{0.44}C_{0.56}$ and $B_{0.24}C_{0.76}$ films selected from the regions A, B and C indicated in Fig. 2(B).

The results obtained from pin-on-disk tests in both rotating and reciprocating modes reveal a similar evolution of the friction coefficient with different carbon contents. In the inset of Fig. 3(A), the linear reciprocating test shows that the friction coefficient drops from 0.66 to 0.13 with increasing the carbon content from 19 to 76 at.%. The wear rate is found to be closely related to the friction coefficient presented in Fig. 3(B). As indicated the wear rate decreases by two orders of magnitude from 6.4×10^{-5} to $1.3 \times 10^{-7} \text{ mm}^3/\text{Nm}$ when the carbon content rises from 19 to 76 at.%. The corrosion characteristics of the M2 substrate with and without the $B_1 - xC_x$ films were assessed by the Potentiodynamic polarization as presented in Fig. 4. Corrosion current density (defined as the current density where the anodic and cathodic reaction rates are equal) and breakdown potential (determined by the potential where the current sharply increases) are very important parameters for the corrosion evaluation. Compared with the bare M2 steel that generally possesses low corrosion resistance, all $B_1 - xC_x$ films studied here appear to significantly improve the corrosion resistance of the substrate. The $B_{0.44}C_{0.56}$ film (region B) with the lowest hardness decreases the corrosion current

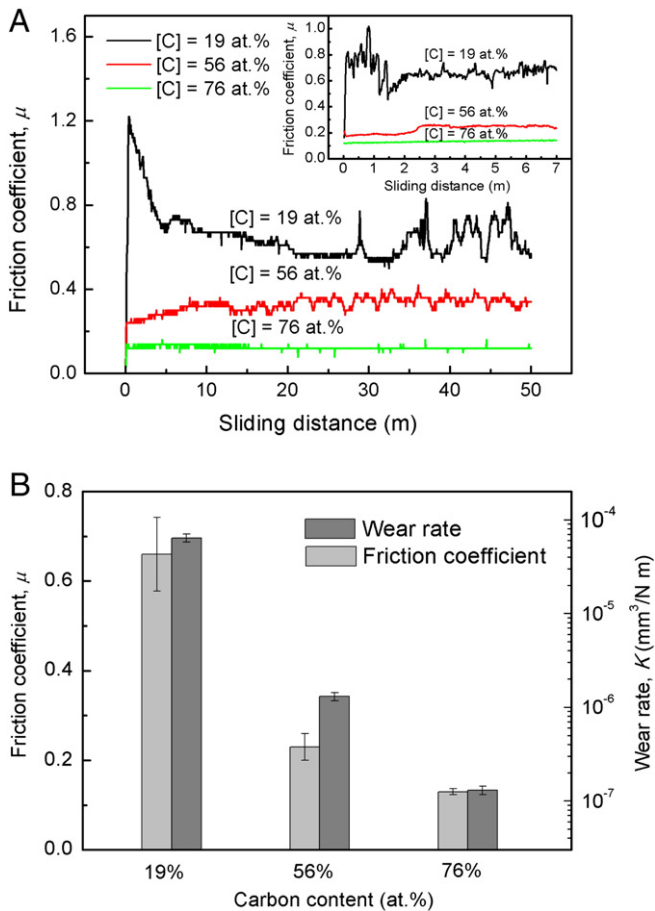


Fig. 3. (A) Friction coefficient, μ , of the $B_1 - xC_x$ films with different carbon contents as a function of the sliding distance measured by a rotating pin-on-disk tribometer. The inset shows the data measured by a linear reciprocating tribometer. (B) Wear rate, K , and friction coefficient, μ , of the $B_1 - xC_x$ films with different carbon contents.

by two orders of magnitude from 3×10^{-6} to 6×10^{-8} A/cm². The boron-rich $B_{0.81}C_{0.19}$ film decreases the corrosion current by four orders of magnitude to 8×10^{-10} A/cm². In addition, the $B_{0.24}C_{0.76}$ film presents a higher breakdown potential of 0.7 V compared with the $B_{0.81}C_{0.19}$ film, which implies the higher resistance to the initiation of localized corrosion, such as pitting.

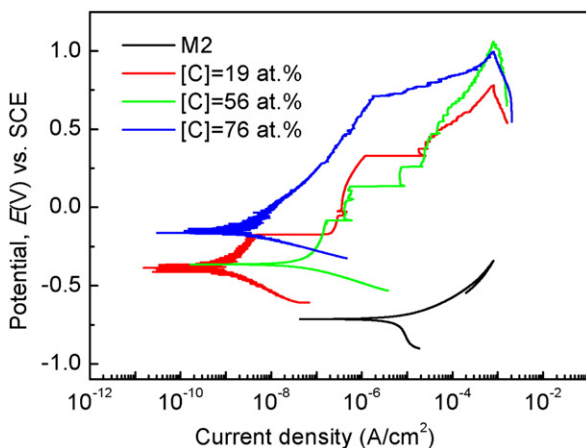


Fig. 4. Potentiodynamic polarization curves of $B_1 - xC_x$ films with different carbon contents.

3.4. Microstructure and composition

In order to explain the characteristics of the $B_1 - xC_x$ materials from regions A, B and C (Fig. 2(B)), we performed a detailed microstructural and chemical analysis using XRD, Raman and XPS measurements. Fig. 5 shows the XRD patterns for the $B_{0.81}C_{0.19}$, $B_{0.44}C_{0.56}$, and $B_{0.24}C_{0.76}$ films selected from the three regions indicated in Fig. 2(B). The patterns without any refined diffraction peaks imply the amorphous nature of the overall structure of the $B_1 - xC_x$ films. The weak and broad diffraction peaks from the $B_{0.81}C_{0.19}$ and $B_{0.24}C_{0.76}$ films suggest formation of nanoparticles of boron carbide imbedded in the amorphous matrix. The diffraction peak at around 37.7° which corresponds to the diffraction from (021) crystallographic planes of boron carbide orthorhombic crystal structure [30] is observed in both the $B_{0.81}C_{0.19}$ and $B_{0.24}C_{0.76}$ films possessing the highest hardness in the A and C regions, respectively. On the other hand, no diffraction peaks are observed in the XRD spectra of $B_{0.44}C_{0.56}$ films exhibiting the lowest hardness (region B). The size of crystallites in the $B_{0.24}C_{0.76}$ film is smaller than that in the $B_{0.81}C_{0.19}$ film as indicated by the broader diffraction peaks. Such small crystallite size can be related to the relatively low boron content for the former film, while the main (021) diffraction peak shifts to higher angles by about 0.2° due to the built-in stress.

Small diffraction peaks at 28.8° and 29.7° are observed in the XRD spectra of $B_{0.81}C_{0.19}$ and $B_{0.24}C_{0.76}$ films, respectively. Referring to the XRD data for bulk boron carbide, weak diffraction peaks are generally observed between 28° and 30°, and their positions vary with composition [31]. Therefore, the small diffraction peaks from $B_{0.81}C_{0.19}$ and $B_{0.24}C_{0.76}$ films may be attributed to boron carbide, but it is difficult to identify their specific phases due to a weak diffraction caused by the amorphous nature of the films and small crystallite size.

In complement to the XRD analysis sensitive to crystallinity, Raman spectroscopy provides information related to the bonding structure. This technique has been frequently applied for the analysis of carbon and carbon-based materials [32,33]. Fig. 6 shows Raman spectra of $B_1 - xC_x$ films with different carbon contents. The $B_{0.81}C_{0.19}$ film (region A, high $H = 28$ GPa) exhibits a broad peak complex between 600 and 1200 cm⁻¹ that can be assigned to the icosahedral mode of boron carbide [10]. In general, no specific peaks are observed in the Raman spectra of boron carbide single crystal at frequencies ranging from 600 to 1200 cm⁻¹ because of the distribution of carbon atoms among the icosahedral sites, which introduces a form of substitutional disorder [10].

As the carbon concentration in the $B_1 - xC_x$ films increases, a broad band between 1000 and 1600 cm⁻¹ arises. This intensity enhancement can be explained by the presence of amorphous carbon, for which the G peak around 1580–1600 cm⁻¹ and the D peak around 1350 cm⁻¹ [34] are characteristic of a mixture of graphitic and disordered sp³-bonded

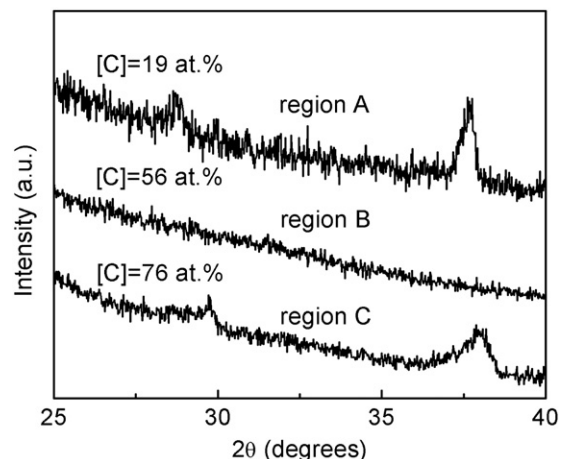


Fig. 5. XRD spectra of the $B_1 - xC_x$ films with different carbon contents.

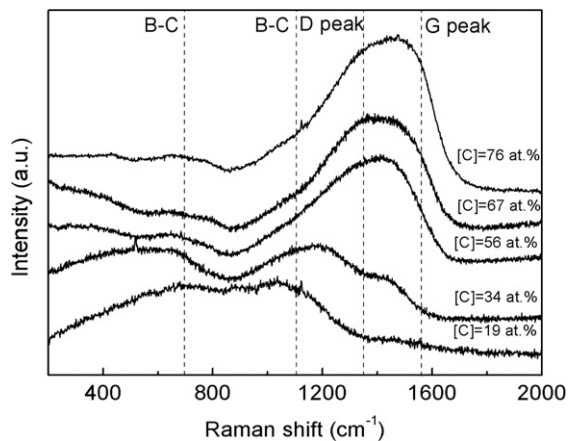


Fig. 6. Raman spectra of the $B_{1-x}C_x$ films with different carbon contents.

carbon [33,35]. Therefore, as the carbon content is increased, the structure can be considered as a mixture of amorphous carbon and boron carbide, as consistently indicated by the XPS analysis.

High resolution XPS core level spectra represented by the B 1s and C 1s peaks were collected to study the impact of carbon content on the chemical states of the $B_{1-x}C_x$ films. Fig. 7 shows typical B 1s and C 1s high resolution spectra of the boron-rich $B_{0.81}C_{0.19}$ and the carbon-rich $B_{0.24}C_{0.76}$ films. The deconvoluted B 1s spectrum of the $B_{0.81}C_{0.19}$ sample in Fig. 7(A) features the presence of two chemical states indicated by the peaks at 188.3 eV and 189.4 eV, which are attributed to the B–C bonds in a B_4C environment (boron-rich), and to the B–C bonds with C atoms in a graphitic state (carbon-rich), respectively [17,36]. An additional

peak at 191.7 eV originating from B–O bonds [37] is observed in the B 1s spectrum of the $B_{0.24}C_{0.76}$ film as shown in Fig. 7(B). The area under each specific deconvoluted peak corresponding to a particular chemical bond structure determines the bond content (see Table 1). Thus when [C] is low the area of the peak centered at 188.3 eV is large which indicates that 78% of carbon participate in the B–C bonds in B_4C . This indicates the presence of the B_4C phase as the major component in such boron-rich films. This observation is consistent with the Raman and XRD results described above.

Curve-fitted C 1s spectra of the selected $B_{0.81}C_{0.19}$ and $B_{0.24}C_{0.76}$ films are presented in Fig. 7(C) and (D). For the boron-rich $B_{0.81}C_{0.19}$ film, the peaks at 282.7 eV in the C 1s spectrum correspond to C–B bonds within the B_4C environment, while a shoulder at 283.9 eV is assigned to B–C bonds in the carbon-rich environment [17,38]. As the carbon content increases, the C 1s peak at 285 eV is significantly higher (as illustrated here for the $B_{0.24}C_{0.76}$ film) indicating an abundant presence of the C–C bonds [18]. Combined with the peak area corresponding to chemical bonding given in Table 1, it is found that further addition of carbon results in an increase of the B–C bonds in the carbon rich-environment as well as in the formation of C–C bonds. This is consistent with the presence of amorphous carbon identified in the Raman spectra of the carbon-rich films.

4. General discussion

In this section, we discuss the mechanical properties of the $B_{1-x}C_x$ films in relation to the changes in the microstructure. In region A the $B_{0.81}C_{0.19}$ film possesses the highest hardness of 28 GPa. In this case the stoichiometry is very close to that of B_4C , and indeed, its X-ray diffraction patterns also indicated the formation of nanocrystalline boron carbide, leading to the high hardness of such film. In region B, no

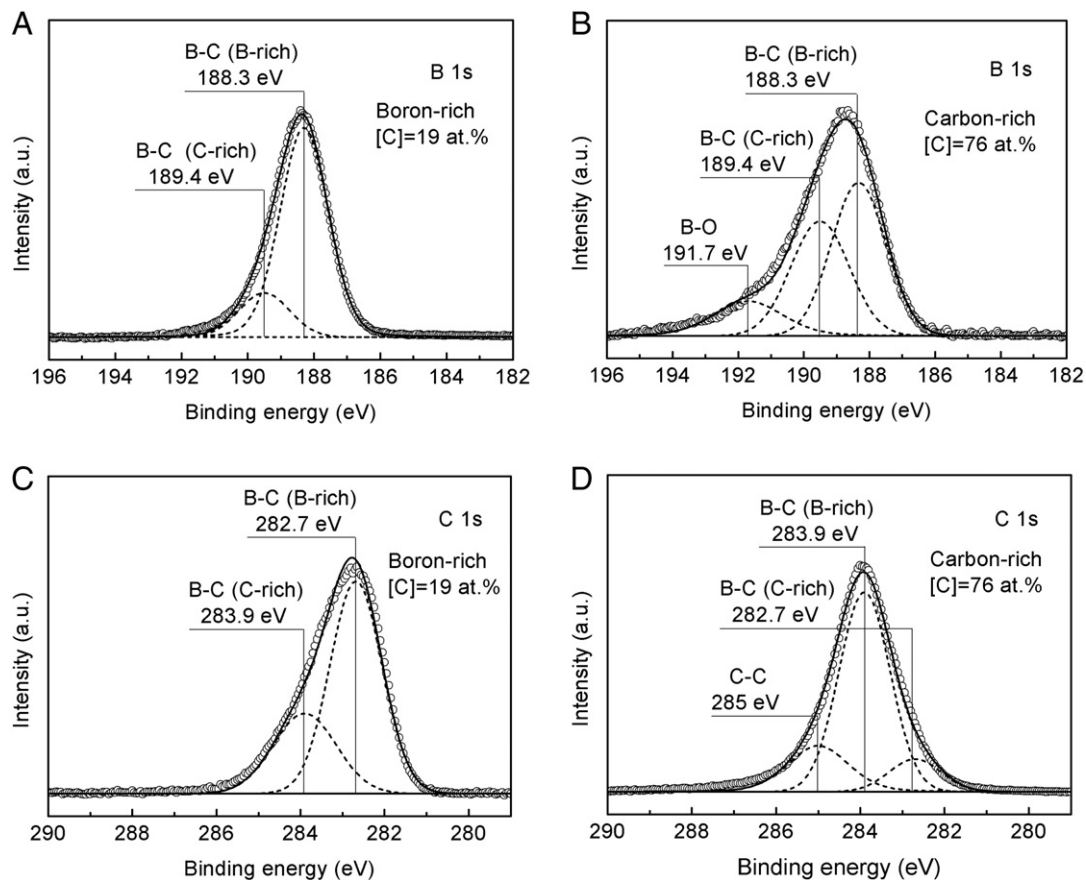


Fig. 7. B1s and C1s core level spectra of the boron-rich $B_{0.81}C_{0.19}$ and the carbon-rich $B_{0.24}C_{0.76}$ films; experimental data (open circles), fitted results (solid lines) and their deconvoluted components (dashed lines).

Table 1

Peak areas corresponding to different chemical bonds in the boron-rich $B_{0.81}C_{0.19}$ and the carbon-rich $B_{0.24}C_{0.76}$ films.

		BE (eV)	Area (%)	
			B _{0.81} C _{0.19} sample	B _{0.24} C _{0.76} sample
B1s	B–C	188.3	82	47
		189.4	18	38
	B–O	191.7	0	15
C1s	C–B	282.7	69	11
		283.9	31	68
	C–C	285.0	0	21

diffraction patterns are observed and the hardness of the $B_1 - xC_x$ films is relatively low. In region C, formation of nanocrystalline boron carbide in the $B_{0.24}C_{0.76}$ film is inferred by XRD, while the presence of amorphous carbon (a-C) is deduced from the Raman spectra. This implies that the microstructure in region C can be described as a nanocomposite consisting of nanocrystalline boron carbide embedded in an amorphous boron carbide/a-C matrix. In this case, we may consider the hardening mechanism in nanocomposite films as described by Veprek [39]; films comprising nanoparticles imbedded in an amorphous matrix, (for example TiN in Si_3N_4) exhibit a high hardness which is enhanced by strengthening the nanoparticle-matrix interfaces [40,41]. Therefore, the structure of nanocrystalline boron carbide in an amorphous boron carbide/a-C matrix also possibly gives rise to a high hardness for relatively low x in $B_1 - xC_x$, specifically, for the $B_{0.24}C_{0.76}$ films ($H = 25$ GPa).

The tribological performance of the $B_1 - xC_x$ films also varies with the composition and microstructure. The friction coefficient and wear rate decrease with the increasing carbon content, which can be related to a higher amount of amorphous carbon indicated by the Raman spectra for the carbon-rich $B_1 - xC_x$ films. The amorphous carbon is the third structure which acts as a solid lubricant during the tribological test, and reduces the friction coefficient and wear rate. As shown, when the hardness is maintained over 25 GPa, the friction coefficient of the $B_1 - xC_x$ films can be adjusted between a high value of 0.66 and a low value of 0.13 by changing the carbon content from 19 to 76 at.%. This feature makes the $B_1 - xC_x$ films very promising to be applied in different areas, where hard coatings with either high or low friction coefficient are demanded.

5. Conclusion

$B_1 - xC_x$ films with tailored carbon content were prepared by magnetron sputtering from element boron and graphite targets. Maximum hardness of 28 and 25 GPa was reached in both boron-rich and carbon-rich regions with [C] of 19 and 76 at.%, respectively. The mechanical properties are explained by the variation in the film microstructure. The structure of the $B_1 - xC_x$ films has generally an amorphous character as deduced from XRD patterns. However, the broad and weak diffraction patterns from boron carbide observed for the films with maximum hardness imply the formation of nanocrystalline boron carbide. Based on the compositional and microstructural analysis by both XPS and Raman techniques, we demonstrate that a nearly stoichiometric B and C ratio like in the boron carbide (B_4C) and presence of a nanocrystalline structure yield the high hardness for boron-rich films. In addition, formation of a nanocomposite structure formed by boron carbide particles imbedded in the amorphous boron carbide/a-C matrix also enhances the high hardness of carbon-rich films.

The friction coefficient of the $B_1 - xC_x$ films decreases from 0.66 to 0.13 by changing the carbon content from 19 to 76 at.% while the hardness over 25 GPa is maintained. The wear rate is correspondingly reduced by two orders of magnitude from 6.4×10^{-5} to 1.3×10^{-7} mm³/Nm. The amorphous carbon component in the carbon-rich

films acts as a solid lubricant layer, and it is responsible for the reduction of the friction coefficient and wear rate. The corrosion resistance of the M2 substrate is also significantly improved by applying the $B_1 - xC_x$ films. Compared with the bare substrate, the corrosion current is reduced by four orders of magnitude to 8×10^{-10} A/cm² when a boron-rich film is used. In addition, $B_{0.24}C_{0.76}$ film gave a better performance with respect to the breakdown potential of 0.7 V. In conclusion, the $B_1 - xC_x$ films with high hardness, tunable tribological properties and high corrosion resistance are promising materials for protective coating in various industrial applications.

Acknowledgements

This work was supported by the Research Grants Council of the Hong Kong Special Administrative Region (Project No. CityU 104911), National Science Foundation of China (NSFC Grant 61176007 and 51372213), and the Natural Sciences and Engineering Research Council of Canada.

References

- [1] S. Ulrich, H. Ehrhardt, J. Schwan, R. Samlenski, R. Brenn, *Diam. Relat. Mater.* 7 (1998) 835.
- [2] Y. Chen, Y.-W. Chung, S.-Y. Li, *Surf. Coat. Technol.* 200 (2006) 4072.
- [3] K. Jagannadham, T.R. Watkins, M.J. Lance, L. Riester, R.L. Lemaster, *Surf. Coat. Technol.* 203 (2009) 3151.
- [4] K. Miyazaki, T. Hagio, K. Kobayashi, *J. Mater. Sci.* 16 (1981) 752.
- [5] M.M. Balakrishnarajan, P.D. Pancharatna, R. Hoffmann, *New J. Chem.* 31 (2007) 473.
- [6] R. Lazzari, N. Vast, J.M. Besson, S. Baroni, A. Dal Corso, *Phys. Rev. Lett.* 83 (1999) 3230.
- [7] H. Werheit, U. Kuhlmann, T. Lundström, *J. Alloy Compd.* 204 (1994) 197.
- [8] B. Morosin, G.H. Kwei, A.C. Lawson, T.L. Aselage, D. Emin, *J. Alloy Compd.* 226 (1995) 121.
- [9] G.H. Kwei, B. Morosin, *J. Phys. Chem.* 100 (1996) 8031.
- [10] D.R. Tallant, T.L. Aselage, A.N. Campbell, D. Emin, *Phys. Rev. B* 40 (1989) 5649.
- [11] V. Domnich, Y. Gogotsi, M. Trenary, T. Tanaka, *Appl. Phys. Lett.* 81 (2002) 3783.
- [12] H. Werheit, *J. Less Common Met.* 67 (1979) 143.
- [13] K.W. Lee, S.J. Harris, *Diam. Relat. Mater.* 7 (1998) 1539.
- [14] M.J. Santos, A.J. Silvestre, O. Conde, *Surf. Coat. Technol.* 151 (2002) 160.
- [15] S. Adenwalla, N. Hong, M.A. Langell, J. Liu, O. Kizilkaya, *J. Appl. Phys.* 107 (2010).
- [16] L.G. Jacobsohn, M. Nastasi, *Surf. Coat. Technol.* 200 (2005) 1472.
- [17] L.G. Jacobsohn, R.K. Schulze, M.E.H.M. da Costa, M. Nastasi, *Surf. Sci.* 572 (2004) 418.
- [18] D.B. Chrisey, R.Q. Bao, *Thin Solid Films* 519 (2010) 164.
- [19] I. Jimenez, I. Caretti, J.M. Albella, *Diam. Relat. Mater.* 16 (2007) 63.
- [20] E. Restrepo-Parra, H.A. Castillo, J.M. Velez, W. de la Cruz, *Surf. Coat. Technol.* 205 (2011) 3607.
- [21] I. Bar, D. Zemsky, R. Shneck, P.J. Dagdigian, *J. Appl. Phys.* 102 (2007).
- [22] J. Podder, M. Rusop, T. Soga, T. Jimbo, *Diam. Relat. Mater.* 14 (2005) 1799.
- [23] O. Postel, J. Heberlein, *Surf. Coat. Technol.* 108 (1998) 247.
- [24] H.Y. Chen, J. Wang, H. Yang, W.Z. Li, H.D. Li, *Surf. Coat. Technol.* 128 (2000) 329.
- [25] H.S. Ahn, P.D. Cuong, K.H. Shin, K.S. Lee, *Wear* 259 (2005) 807.
- [26] T. Eckardt, K. Bewilogua, G. van der Kolk, T. Hurkmans, T. Trinh, W. Fleischer, *Surf. Coat. Technol.* 126 (2000) 69.
- [27] W.C. Oliver, G.M. Pharr, *J. Mater. Res.* 7 (1992) 1564.
- [28] M.P.M. Azzi, J.E. Klemberg-Sapieha, L. Martinu, the 52th annual SVC conference, Society of Vacuum Coaters, Santa-Clara USA, 2009.
- [29] J. Musil, F. Kunc, H. Zeman, H. Poláková, *Surf. Coat. Technol.* 154 (2002) 304.
- [30] O. Conde, A.J. Silvestre, J.C. Oliveira, *Surf. Coat. Technol.* 125 (2000) 141.
- [31] R.M. Mohanty, K. Balasubramanian, S.K. Seshadri, *J. Alloy Compd.* 441 (2007) 85.
- [32] K. Yamamoto, M. Keuncke, K. Bewilogua, Z. Czigany, L. Hultman, *Surf. Coat. Technol.* 142 (2001) 881.
- [33] B. Todorovi-Markovic, I. Draganic, D. Vasiljevic-Radovic, N. Romcevic, M. Romcevic, M. Dramicanin, Z. Markovic, *Appl. Surf. Sci.* 253 (2007) 4029.
- [34] A.C. Ferrari, J. Robertson, *Phys. Rev. B* 61 (2000) 14095.
- [35] H. Neuhauser, U. Harms, M. Gaertner, A. Schutze, K. Bewilogua, *Thin Solid Films* 385 (2001) 275.
- [36] W. Cermignani, T.E. Paulson, C. Onneby, C.G. Pantano, *Carbon* 33 (1995) 367.
- [37] S. Jacques, A. Guette, X. Bourrat, F. Langlais, C. Guimon, C. Labrugere, *Carbon* 34 (1996) 1135.
- [38] C. Ronning, D. Schwen, S. Eyhusen, U. Vetter, H. Hofsäss, *Surf. Coat. Technol.* 158–159 (2002) 382.
- [39] S. Veprek, S. Reiprich, S.H. Li, *Appl. Phys. Lett.* 66 (1995) 2640.
- [40] S. Veprek, M.G.J. Veprek-Heijman, P. Karvankova, J. Prochazka, *Thin Solid Films* 476 (2005) 1.
- [41] S. Veprek, *J. Vac. Sci. Technol. A* 17 (1999) 2401.